Protective Coating of Single-Crystalline Ni-Rich Cathode Enables Fast Charging in All-Solid-State Batteries

Wengao Zhao[1,*], Ruizhuo Zhang[1], Fucheng Ren[2], Leonhard Karger[1], Sören L. Dreyer[1], Jing Lin[1], Yuan Ma[1,3,*], Yong Cheng[2], Avnish Singh Pal[4,5], Martin Velazquez-Rizo[4,5], Ali Ahmadian[4,6], Ziyan Zhang[1], Philipp Müller[7], Jürgen Janek[1,8], Yong Yang[2], Aleksandr Kondrakov[1,7], Torsten Brezesinski[1,*]

[1]Battery and Electrochemistry Laboratory (BELLA), Institute of Nanotechnology, Karlsruhe Institute of Technology (KIT), Kaiserstr. 12, 76131 Karlsruhe, Germany

Email: wengao.zhao@kit.edu, torsten.brezesinski@kit.edu

[2]State Key Laboratory for Physical Chemistry of Solid Surfaces, College of Chemistry and Chemical Engineering, Xiamen University, Xiamen 361005, China

[3]Confucius Energy Storage Lab, School of Energy and Environment, Southeast University, Nanjing, China

Email: yuan.ma@seu.edu.cn

[4]Institute of Nanotechnology, Karlsruhe Institute of Technology (KIT), Kaiserstr. 12, 76131 Karlsruhe, Germany

[5]Karlsruhe Nano Micro Facility (KNMFi), Karlsruhe Institute of Technology (KIT), Kaiserstr. 12, 76131 Karlsruhe, Germany

[6]Helmholtz Institute Ulm (HIU) for Electrochemical Energy Storage, Helmholtzstr. 11, 89081 Ulm, Germany

[7]BASF SE, Carl-Bosch-Str. 38, 67056 Ludwigshafen, Germany

[8]Institute of Physical Chemistry & Center for Materials Research (ZfM/LaMa), Justus-Liebig-University Giessen, Heinrich-Buff-Ring 17, 35392 Giessen, Germany

Abstract

Improving interfacial stability between cathode active material (CAM) and solid electrolyte (SE) is vital for developing high-performance all-solid-state batteries (ASSBs), with compatibility issues among the cell components representing a major challenge. CAM surface coating with a chemically inert ion conductor is a promising approach to suppress side reactions occurring at the cathode interfaces. Another strategy to mitigate mechanical degradation involves utilizing single-crystalline particle morphologies. Their more robust bulk structure and lower tortuosity for charge transport, compared to polycrystalline (PC) CAMs, can significantly enhance

cyclability in ASSBs. Herein, we coated a $LiNbO_3$ protective layer onto the free surface of quasi single-crystalline $LiNi_{0.83}Co_{0.12}Mn_{0.05}O_2$ (SC83) particles. Pellet-stack ASSB cells using the $LiNbO_3$@SC83 CAM and argyrodite Li_6PS_5Cl as SE showed a capacity retention of 88% after 1000 cycles at 1C rate, compared to only 71% for the uncoated counterpart and far superior to that of $LiNbO_3$@PC83 (30%). The effectiveness of $LiNbO_3$ coating and the SC-NCM nature in mitigating electro-chemo-mechanical degradation was studied by combining modeling and physical/electrochemical characterizations. We demonstrate that the capacity decay at fast charge is due primarily to the mechanical degradation of CAM particles, while it is strongly determined by CAM|SE interfacial reactions under slow-charging conditions.

Keywords: Interfacial stability, protective coating, electro-chemo-mechanical degradation, thiophosphate solid electrolyte, Ni-rich layered oxide cathode

Introduction

Rechargeable lithium-ion batteries (LIBs) are being extensively used in portable electronics and electric vehicles.[1-3] However, conventional LIBs are subjected to potential safety issues and constrained energy density, as they make use of flammable, liquid electrolytes and graphite as the anode.[4, 5] All-solid-state batteries (ASSBs) are regarded as promising next-generation energy-storage devices, owing to the integration of inherently non-flammable, inorganic solid electrolytes (SEs) and high-capacity Li metal at the anode side, ultimately tackling safety issues and boosting energy density.[6, 7] Notably, ASSBs are capable of suppressing cross-talk effects, which may widen the field of application and further helps improve cycle life.[8, 9]

Sulfide-based ASSBs are recognized as one of the most promising systems, primarily because of the easy processing of thiophosphate SEs, even allowing for cold pressing (ensuring good interfacial contact with the CAM particles), and the fact that their ion conductivity is similar to that of common liquid electrolytes (e.g., Li_6PS_5Cl, $\sigma_{ion} \approx 3$ mS/cm at 25 °C).[10, 11] The main drawback is the limited longevity of sulfide-based ASSBs, due to aging induced by various degradation processes. Mechanical degradation due to particle fracture and contact loss in high-energy-density cells using Ni-rich $LiNi_xCo_yMn_zO_2$ (NCM or NMC, with $x \geq 0.8$) CAMs is a

severe issue, leading to accelerated capacity fading.[12, 13] Moreover, thiophosphate SEs have a narrow electrochemical stability window and relatively poor compatibility with NCMs, in particular at high potentials or, in other words, at high states of charge.[14, 15] Therefore, implementing Ni-rich NCMs with both a robust bulk structure and an effective surface protection appears to be necessary for pushing sulfide-based ASSBs toward commercial applications.

Single-crystalline NCMs (SC-NCMs) can provide superior cycling stability in ASSBs by preventing crack formation and maintaining good contact with the SE particles, by reason of their quasi grain-boundary-free structure.[11, 16, 17] Aside from that, CAM|SE side reactions should be mitigated because of the presence of an inert surface coating.[18] $LiNbO_3$ has been widely used for this purpose. The results show effective stabilization of thiophosphate SEs, inhibiting their decomposition (chemical/electrochemical oxidation) and preventing oxygen release from the NCM lattice.[19, 20] Modeling also confirms that $LiNbO_3$ can serve as a promising physical isolation layer, as it is compatible with thiophosphate SEs and exhibits a high ionic (lithium) but low electronic conductivity.[21, 22] Overall, $LiNbO_3$ coatings in ASSBs have been extensively investigated, including tailoring of crystallinity and thickness (content).[23-27] However, most studies focused on the performance improvements achieved using $LiNbO_3$-coated CAMs, while in-depth understanding of degradation mechanisms is largely lacking.[28, 29] To the best of our knowledge, correlations between interfacial side reactions, bulk structural evolution, and cyclability of surface-protected Ni-rich SC-NCM composite cathodes have not yet been investigated in detail.

Herein, we report on sulfide-based ASSBs using a $LiNbO_3$-coated Ni-rich SC-NCM, namely $LiNi_{0.83}Co_{0.12}Mn_{0.05}O_2$ (referred to as SC83 hereafter). The coating was applied onto the CAM particles via a sol-gel approach. To understand the improvement achieved by using $LiNbO_3$ as a coating material, the rate and long-term cycling performance of bare (uncoated) SC83, $LiNbO_3$@SC83, and their counterparts, polycrystalline $LiNi_{0.83}Co_{0.12}Mn_{0.05}O_2$ (PC83) and $LiNbO_3$@PC83, were systematically investigated in In/InLi|Li_6PS_5Cl|CAM cells. We note that the cathode also contained carbon black (1 wt.%), in addition to SE (30 wt.%). The $LiNbO_3$-coated NCMs are found to show enhanced rate capability and cycle life, among others due to

mitigation of adverse side reactions and retention of lithium transport paths. In particular, cells using the $LiNbO_3$@SC83 are capable of achieving 88% capacity retention after 1000 cycles at 1C (among the best cycling performances of sulfide-based ASSBs reported to date), far superior to that with SC83, PC83, or $LiNbO_3$@PC83.

Results and Discussion

Figures 1a and **S1** (Supporting Information) show scanning electron microscopy (SEM) images at different magnifications of the coated and uncoated SC83 particles, indicating that they have an average size of 3.6 μm (with a minor fraction of smaller particles) and a rather clean surface. A sol-gel method was used to coat the CAM particles with $LiNbO_3$ from ethoxide precursors, followed by calcination at 350 °C under O_2 atmosphere.[30] The fact that a conformal coating is formed on the surface of the single-crystalline particles is evident from the higher-magnification SEM image in **Figure 1b**.

Both PC83 and $LiNbO_3$@PC83 were prepared accordingly, with respective SEM images presented in **Figure S2**.[5] In that case, the CAM secondary particles have an average size of 3.5 μm, which is almost identical to that of SC83. Rietveld refinement analysis of X-ray diffraction (XRD) data collected from $LiNbO_3$@SC83 (**Figure 1c**) revealed a well-layered structure with minor Li^+/Ni^{2+} cation mixing. The same is true for the other materials (**Figure S3**), all of which exhibit low fractions of $Ni^{\bullet}_{Li}$ point defects. The relevant structural parameters are given in **Table S1**.

Scanning transmission electron microscopy (STEM) and energy dispersive X-ray spectroscopy (EDS) mapping (**Figure 1d**) further corroborated the presence of a relatively uniform layer containing Nb and O of thickness about 10 nm on the surface of SC83. Higher-resolution imaging (**Figure 1e**,**f**) confirmed the (local) layered bulk structure, as well as the poor crystallinity of the Li-Nb-O coating. The interface between the SC83 and the coating is clearly visible from the respective images. The distance of 2.04 Å corresponds to the interplanar spacing of the (0−14) crystal plane of NCM ($R-3m$ space group), while those of 2.33 and 1.53 Å are consistent with the spacings of the (−123) and (030) planes of $LiNbO_3$ ($R-3c$ space group).

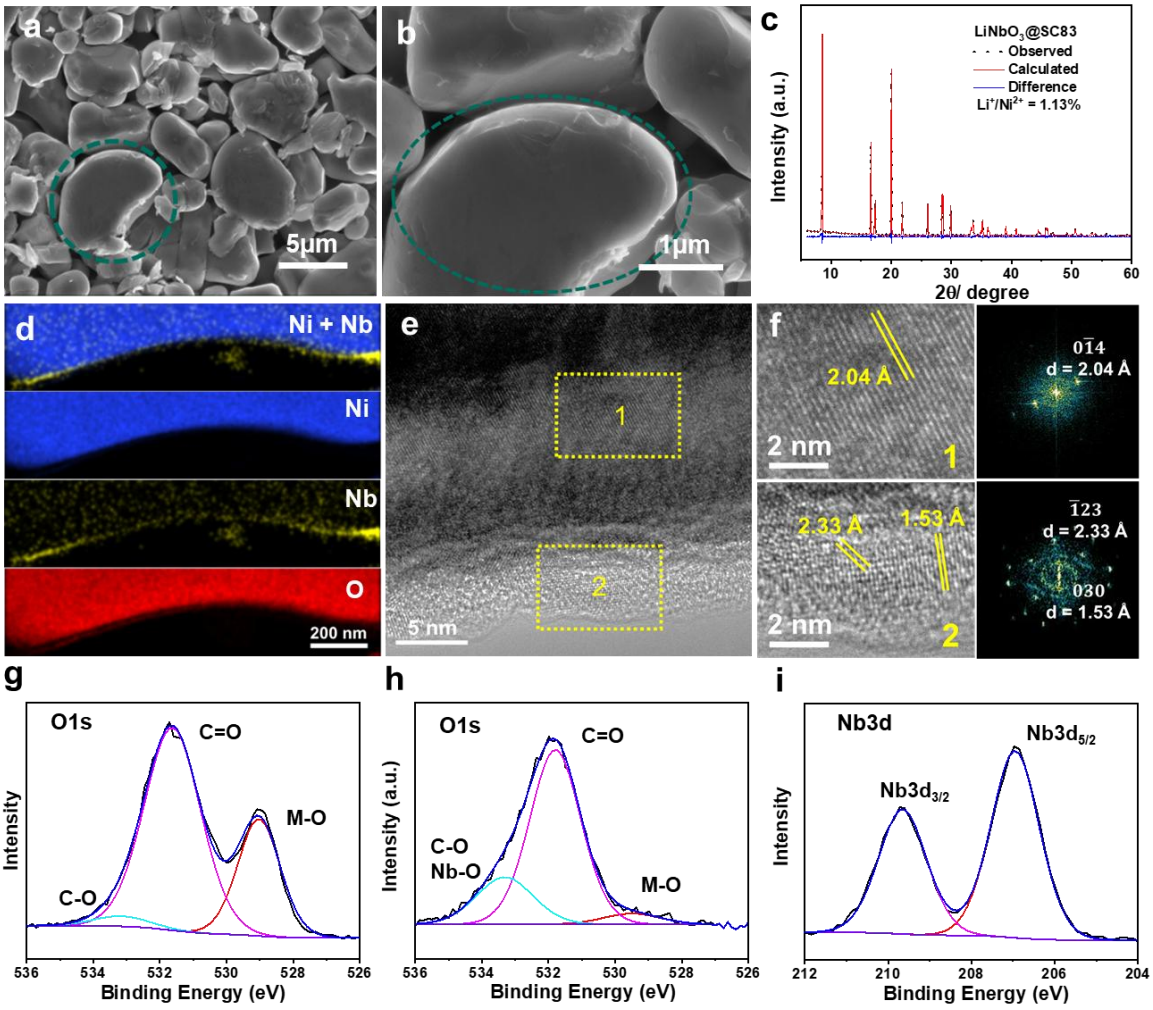

Figure 1. Morphology, structure, and surface properties of the coated and uncoated SC83 CAMs. (a,b) SEM images at different magnifications of $LiNbO_3$@SC83. (c) XRD pattern of $LiNbO_3$@SC83 with corresponding Rietveld analysis. (d) Element mapping of $LiNbO_3$@SC83 and (e,f) corresponding surface/bulk phase identification via STEM and fast Fourier transform (FFT) analysis. XPS detail spectra of the (g) O 1s core level of SC83 and (h) O 1s and (i) Nb 3d core levels of $LiNbO_3$@SC83.

X-ray photoelectron spectroscopy (XPS) data were also collected from the samples to gain insight into the $LiNbO_3$ formation by focusing on O and Nb present on the surface of SC83. Specifically, the O 1s and Nb 3d core level regions were examined (**Figure 1g–i**), with the former showing three characteristic peaks at binding energies of 533.5, 531.8, and 529.2 eV, corresponding to C–O/Nb–O, C=O, and Ni/Co/Mn–O (referred to as M–O in the following), respectively.[31, 32] The C=O and C–O signals likely originate from residual lithium (e.g., in the

form of carbonates) from the preparation process, while the M–O signal can be attributed to lattice oxygen. Compared to SC83, a more intense C–O/Nb–O peak is observed for the $LiNbO_3$@SC83 due to surface coating. In addition, the decrease in intensity of the M–O peak is a clear indication of particle coverage. The C=O peak remains largely unaltered. Moreover, the Nb 3d data of $LiNbO_3$@SC83 show a distinct doublet, thus corroborating the presence of Nb^{5+}.[33, 34]

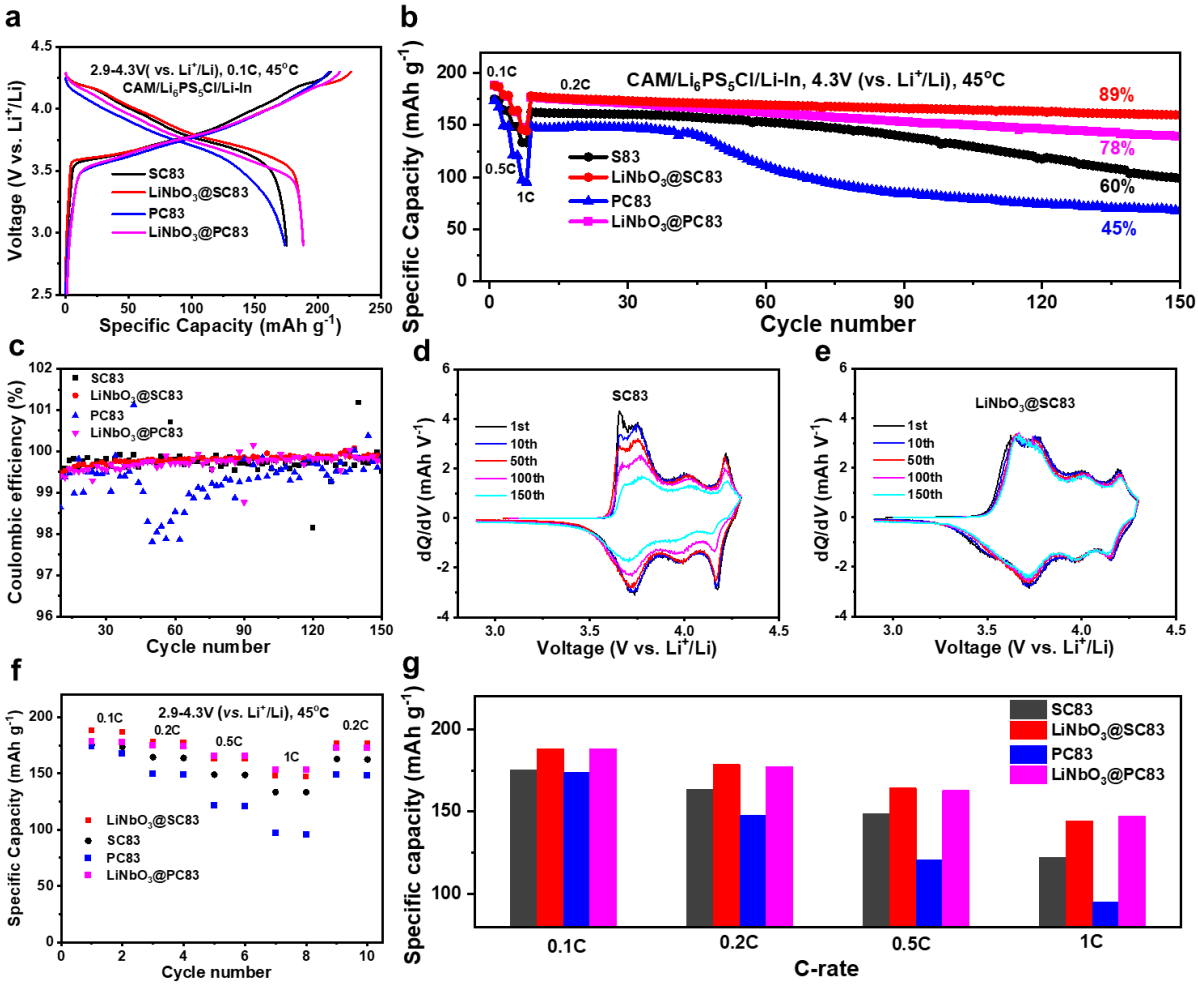

Figure 2. Cathode performance in sulfide-based ASSBs. (a) First-cycle voltage profiles at 0.1C and 45 °C, (b) long-term cycling stabilities at 0.2C, and (c) corresponding Coulomb efficiencies. Differential capacity curves of the 1st, 10th, 50th, 100th, and 150th cycles for (d) SC83 and (e) $LiNbO_3$@SC83. (f) Rate capabilities and (g) corresponding specific capacities at C-rates ranging from 0.1C to 1C.

The electrochemical performance of the bare and coated CAMs in sulfide-based ASSBs with a

high (theoretical) areal loading of about 2 mAh/cm^2 was evaluated to verify the effect of the $LiNbO_3$ coating. Both $LiNbO_3$@PC83 and $LiNbO_3$@SC83 delivered similar but higher first-cycle specific discharge capacities than SC83 and its counterpart PC83 (~190 vs. 175 mAh/g at 0.1C rate and 45 °C, **Figure 2a**). As expected, the coated cathodes exhibited higher initial Coulomb efficiencies [(83–87)% vs. (80–83)%], as detailed in **Table S2**. Long-term cyclability testing (**Figures 2b** and **S4**) revealed that $LiNbO_3$@SC83 indeed achieves the best capacity retention of 89% after 150 cycles at 0.2C rate, while SC83, PC83, and $LiNbO_3$@PC83 show capacity retentions of 60, 45, and 78%, respectively. Evidently, the combination of SC83 with its robust bulk structure and $LiNbO_3$ with its high ionic conductivity leads to a synergistic effect,[35] helping to suppress bulk/surface degradation by preventing CAM|SE side reactions. The related variations in Coulomb efficiency are shown in **Figure 2c**. As can be seen from the data, the $LiNbO_3$@SC83 and $LiNbO_3$@PC83 cells displayed the highest Coulomb efficiencies throughout cycling, while SC83 and PC83 showed some unexpected fluctuations. The faster stabilization is additional evidence that the degradation processes are effectively mitigated.

To further verify the reversibility of phase transitions induced by lithium (de)intercalation during long-term cycling, dQ/dV curves were examined (**Figures 2d**,**e** and **S5**). All CAMs undergo similar (reversible) phase transitions (H1-M-H2-H3).[36-38] It should be noted that irreversible phase transitions induce severe lattice strain and cause microcrack formation inside the particles, eventually resulting in contact loss and capacity decay.[39] Clearly, $LiNbO_3$@SC83 shows superior reversibility of the H2-H3 transition, signifying its lower strain accumulation compared to the other CAMs. The rate capability testing of the different cathodes at 0.1C, 0.2C, 0.5C, and 1C is shown in **Figure 2f**,**g**. As evident, the $LiNbO_3$@PC83 and $LiNbO_3$@SC83 cells exhibited a similar performance, better than that of SC83 and PC83. At 1C, both coated CAMs delivered a specific capacity of about 150 mAh/g, while the bare materials performed much worse, with specific discharge capacities of 130 mAh/g for SC83 and 100 mAh/g for PC83. To quantitatively compare the increase in overpotential with increasing C-rate, representative voltage profiles are shown in **Figure S6**. $LiNbO_3$@SC83 had a somewhat lower voltage drop and overpotential than SC83 upon increasing the C-rate from 0.5C to 1C, indicating that the latter material also provides a reasonable interface stability in the initial cycles.[40, 41] In contrast,

PC83 shows a significantly increased polarization at 0.5C and 1C. The differences are due to the following: 1) Limited ion and electron transport because of intergranular particle fracture induced by anisotropic volume variations during cycling, and 2) severe CAM|SE side reactions, which can also cause crack formation near the particle surface (followed by propagation into the bulk).

In summary, $LiNbO_3$ coating is found to significantly mitigate polarization by suppressing detrimental interfacial reactions. However, this kind of stabilization is much more pronounced when combined with the high mechanical stability of single-crystalline cathodes.

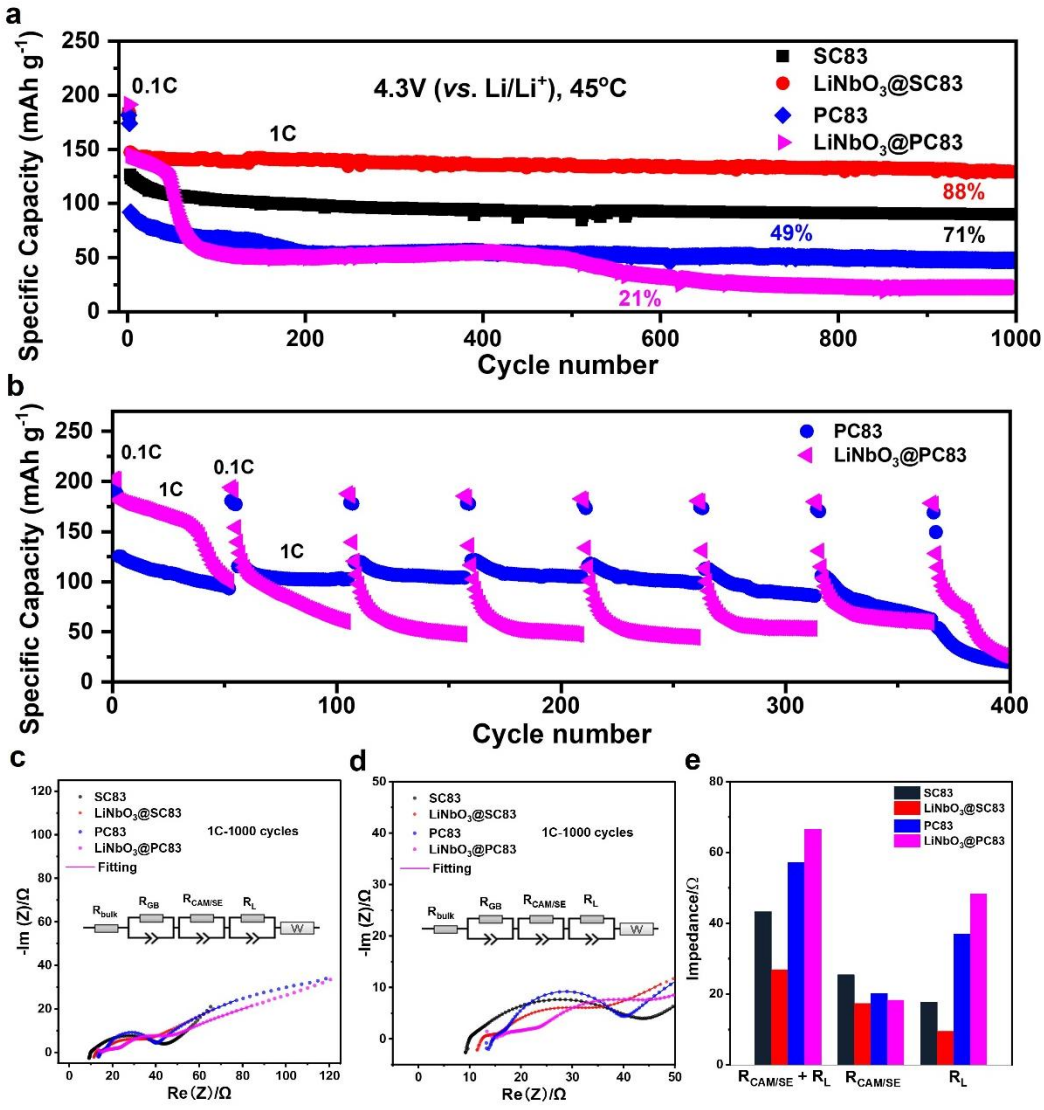

Figure 3. Cycling stability of the composite cathodes in sulfide-based ASSBs. (a) Long-term performances at 1C. (b) Comparison of cyclability of PC83 and $LiNbO_3$@PC83, with 0.1C steps after every 50 cycles at 1C. (c,d) EIS analysis after 1000 cycles at 1C and (e) summary of

extracted resistances.

To learn more about the effectiveness of the protective coating, ASSB cells having the same areal loading were cycled for 1000 cycles at 1C rate. As shown in **Figures 3a** and **S7**, both the SC83 and $LiNbO_3$@SC83 cells exhibited high-capacity retentions of ~71 and 88%, respectively, far superior to that of PC83 (49%) and $LiNbO_3$@PC83 (21%). Accordingly, they showed minor capacity losses per cycle (0.029 and 0.012%), which in the case of SC83 were even lower as compared to the 0.2C cycling in **Figure 2b**. This may be due to the shorter time spent at high potentials in each cycle.[14] A comparison of cycling performances and capacity retentions of sulfide-based ASSBs is given in **Table S3**. Evidently, $LiNbO_3$@SC83 is capable of maintaining better stability than most of the NCM CAMs reported in the literature up until now.

For better understanding the factors that determine the stability of PC83 and $LiNbO_3$@PC83, the cells were evaluated at 1C and with low C-rate testing (0.1C) every 50 cycles up to 400 cycles after two initial (formation) cycles at 0.1C (**Figure 3b**). $LiNbO_3$@PC83 displayed a sharp decay after about 40 cycles, after which the specific discharge capacity recovered to 170–180 mAh/g upon changing the C-rate back to 0.1C (comparable to the initial capacities). Notably, PC83 delivered higher capacities than $LiNbO_3$@PC83 from the 50th cycle onward. This is likely because of the lower state of charge (SOC) in the initial cycles, helping to maintain the particle morphology and structure upon long-term cycling. Interestingly, the cells showed the same behavior over hundreds of cycles due to sluggish charge transport within the fractured but still interconnected CAM particles. Specifically, ion/electron transport is hampered by the random orientation of primary particles and cracking along the grain boundaries in polycrystalline NCMs. This is much less of a problem with single-crystal NCMs (more robust structure, lower tortuosity for charge transport, etc.).[11, 42] However, the effect that the effective transport pathways have on cyclability and stability can be somewhat controlled by optimizing the rate of charging (current density). In summary, one can conclude that sluggish charge transport at high C-rates is a major problem in PC-NCM-based ASSBs.

Electrochemical impedance spectroscopy (EIS) measurements were also conducted on the cathodes to examine the CAM|SE evolution and its effect on cell resistance. **Figure 3c** shows

Nyquist plots of the electrochemical impedance, along with curve fits, after 1000 cycles at 1C rate, with a magnified view shown in **Figure 3d**. The equivalent circuit model used for fitting is presented in the inset. To differentiate between different kinetic processes, a distribution of relaxation times (DRT) analysis was conducted (**Figure S8**). The fitting results highlight the various contributions to resistance, namely bulk SE (R_{bulk}), SE grain boundary (R_{GB}), CAM|SE ($R_{CAM|SE}$), and charge-transfer resistance at the cathode interface overlapping with the anode contribution in the low-frequency region (R_L). A Warburg element was used to represent the diffusion polarization. The resistances were distinguished based on the calculated time constants, with the fitting parameters given in **Table S4**. As can be seen, the $LiNbO_3$ coating indeed offers several benefits. Both the $LiNbO_3$@PC83 and $LiNbO_3$@SC83 cells exhibit lower interfacial resistances ($R_{CAM|SE}$) than their uncoated counterparts, primarily due to reduced side reactions. Notably, the mechanically superior SC83 cathodes show much less hindrance to charge transfer compared to that of the PC83 cathodes. For instance, $LiNbO_3$@PC83 displays more than five times the R_L than $LiNbO_3$@SC83 (9.5 vs. 48.3 Ω). While the anode contributes to the overall interfacial charge-transfer resistance (R_L), the stability of the In/InLi anode ensures longevity, as demonstrated here.[6, 13]

Taken together, the presence of the chemically inert coating, coupled with the favorable bulk properties of SC83, results in the lowest interfacial resistance ($R_{CAM|SE} + R_L$) among the composite cathodes tested, and as detailed above, enables high specific discharge capacities and excellent capacity retention over hundreds of cycles in sulfide-based ASSBs.

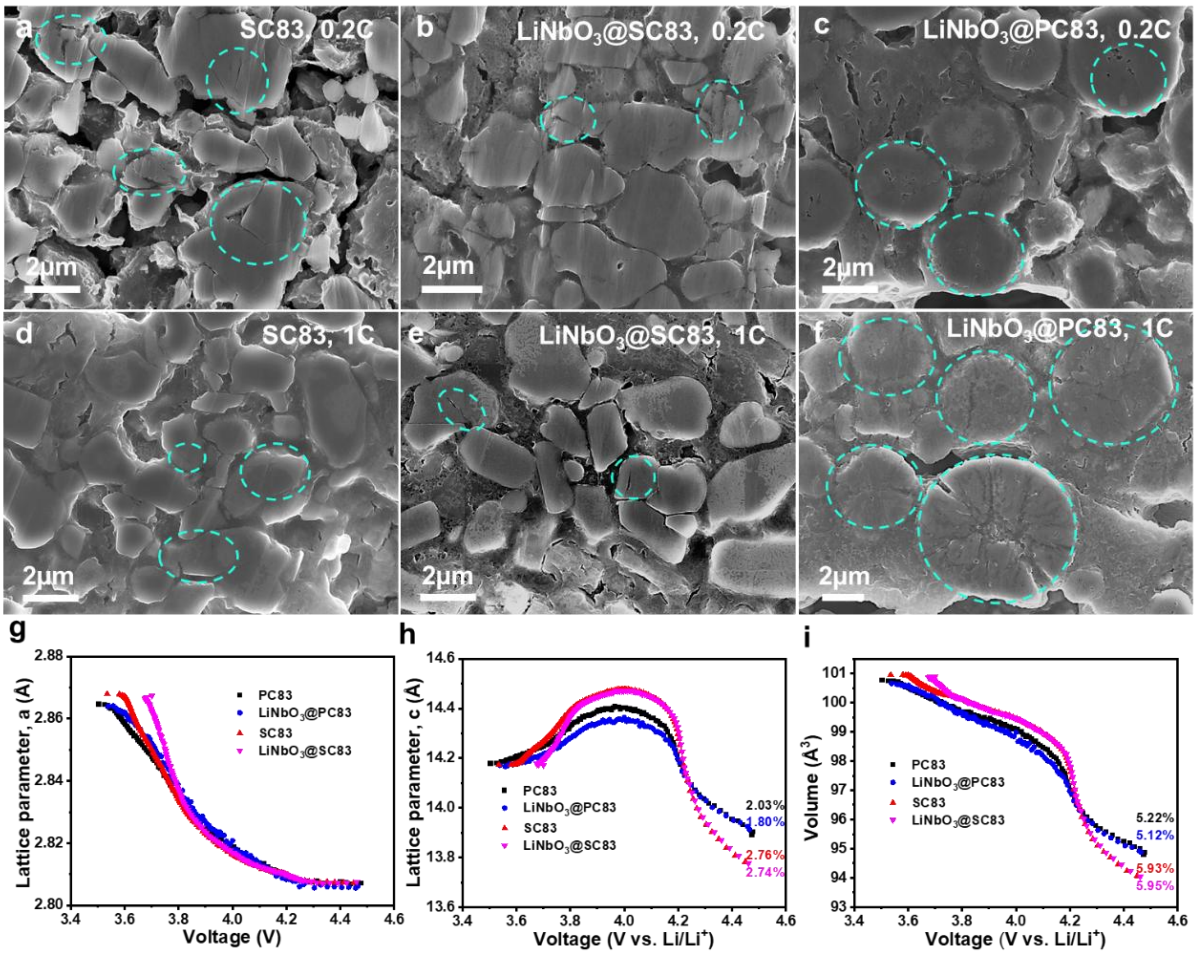

Figure 4. Bulk structural stability of the composite cathodes in sulfide-based ASSBs. Cross-sectional SEM images of (a,d) SC83, (b,e) $LiNbO_3$@SC83, and (c,f) $LiNbO_3$@PC83 after 150 cycles at 0.2C or 1000 cycles at 1C, respectively. (g–i) Changes in lattice parameters and cell volume of the different CAMs from *operando* XRD of the first cycle in conventional Li-ion half-cells.

The cycled cathodes were further harvested from the cells and then imaged by electron microscopy. Unlike $LiNbO_3$@SC83, the *ex situ* cross-sectional SEM images of the SC83, PC83, and $LiNbO_3$@PC83 particles after 150 cycles at 0.2C rate showed visible cracking (**Figures 4a–c** and **S9**). Note that a robust bulk structure ensures fast and stable Li-ion transport inside the electrode and helps suppress contact loss between the CAM and the SE. Moreover, it was attempted to explore the improvement in cyclability by examining the stability of the CAMs after 1000 cycles at 1C rate (**Figures 4d–f** and **S10**). Both SC83 and $LiNbO_3$@SC83 showed

minor cracking, the reason being the negligible internal particle strain, due to the quasi grain-boundary-free structure. In addition, the lower SOC leads to less volume changes during battery operation. Overall, both factors result in a well-maintained bulk structure.[5, 43] In contrast, PC83 and $LiNbO_3$@PC83 suffered from severe cracking, which can be attributed to non-uniform lithium distribution and build-up of strain in the polycrystalline CAM particles.[44] Interestingly, $LiNbO_3$@PC83 displayed more severe cracking at 1C, suggesting that the C-rate also affects, to some degree, the degradation behavior.[45, 46]

To find out if particle fracture is directly correlated to cell volume variations during cycling, *operando* XRD measurements were carried out. The obtained data were refined to extract the changes in lattice parameters *a*, *c* and cell volume *V* on the first cycle in conventional LIB half-cells. For all materials, the lattice parameter *a* decreased similarly during charge, although the open-circuit voltage and onset potential were different due to differences in polarization/CAM surface composition (**Figure 4g**). In contrast, the lattice parameter *c* increased up to 4.0 V vs. Li^+/Li and then decreased strongly at higher potentials. Both SC83 and $LiNbO_3$@SC83 showed similar changes in lattice parameters *a*, *c*, with *c* experiencing larger overall changes compared to PC83 and $LiNbO_3$@PC83 (**Figure 4h**). The reason for this is due in part to the higher specific charge capacity of SC83 and $LiNbO_3$@SC83 in the potential window of 2.9–4.5 V (**Figure S11**), leading to higher degrees of delithiation. In polycrystalline CAM particles, cracking is inevitable due to volume expansion/shrinkage (breathing) of the randomly oriented primary particles. Both PC83 and $LiNbO_3$@PC83 showed more severe cracking, especially at 1C rate after 1000 cycles, although they suffered from less volume variations, as indicated in **Figures 4a–i**, **S9**, and **S10.** These findings further confirm that the presence of grain boundaries in CAMs (rather than mechanical toughness) accounts for the crack formation. Internal cracks block the ion and electron transport (in absence of electrolyte), which in turn aggravates local strain due to non-uniform lithium distribution, thereby exacerbating crack propagation, i.e., mechanical degradation, and resulting in capacity decay (**Figure 3a**).[11, 17, 44] It is worth noting that PC83 showed more pronounced mechanical degradation than $LiNbO_3$@PC83. In uncoated, layered Ni-rich oxides, the Li-deficient phases formed on the CAM surface can react with the SE, causing electrolyte oxidation and CAM reduction to rock-salt type NiO. The latter can

accelerate mechanical failure and leads to continuous degradation, from the surface to the bulk.[29, 47] Therefore, a protective coating and grain-boundary-free particles are necessary for preserving the bulk and surface properties (structure) during prolonged cycling.[13, 39, 48]

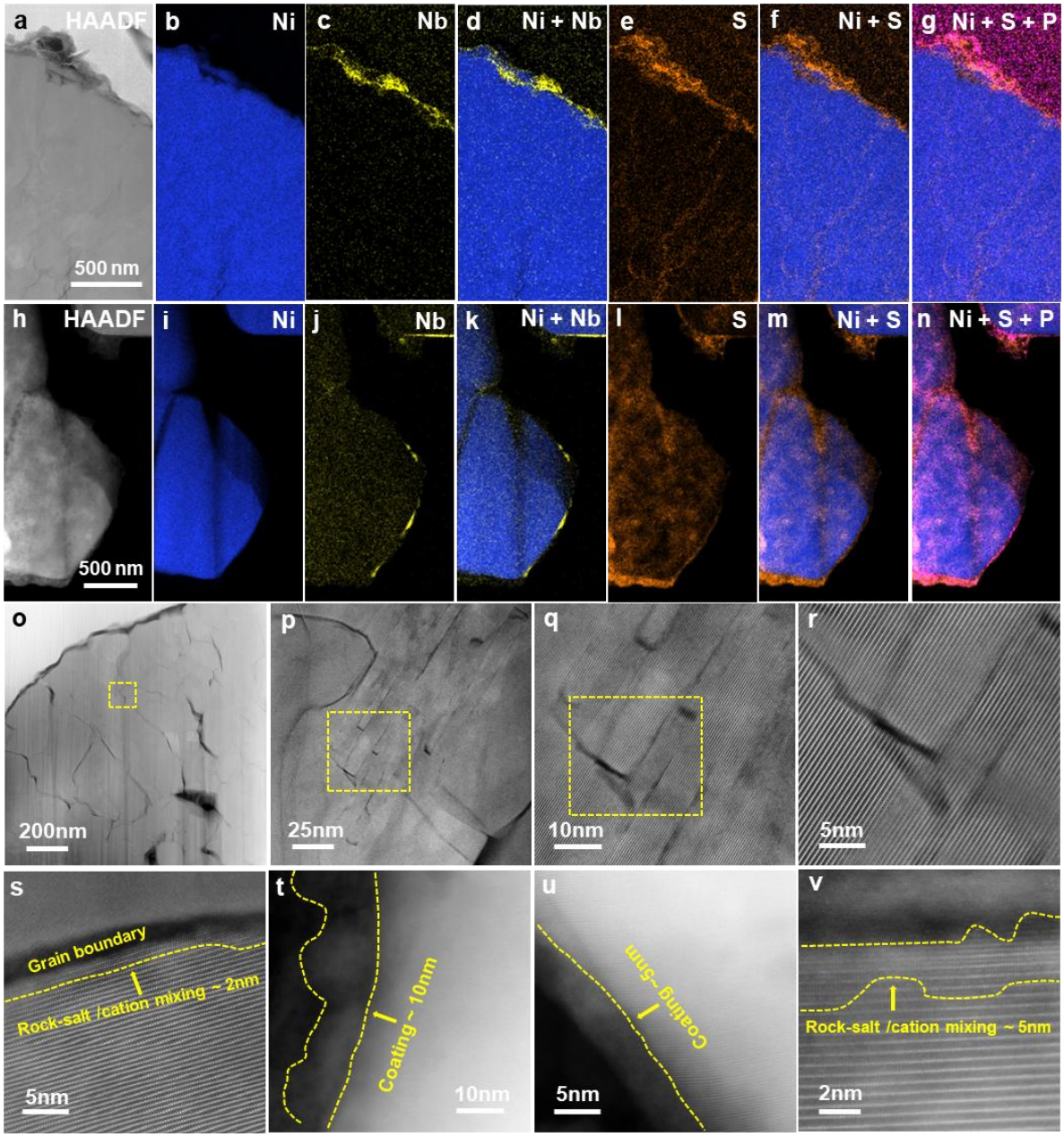

Figure 5. Mechanical degradation of the composite cathodes in sulfide-based ASSBs after 1000 cycles at 1C. Elemental maps of (a–g) $LiNbO_3$@PC83 and (h–n) $LiNbO_3$@SC83. STEM images at different magnifications of (o–t) $LiNbO_3$@PC83, (u) $LiNbO_3$@SC83, and (v) SC83.

As discussed above, the $LiNbO_3$ coating helps mitigate electro-chemo-mechanical degradation. In addition to SEM, TEM measurements were conducted on the coated CAMs after 1000 cycles

at 1C rate to assess potential changes to the surface. The EDS maps in **Figure 5a–d**,**h–k** demonstrate that the protective coating is largely retained during cycling. The higher-magnification elemental distribution maps in **Figure S12** confirm that the Nb-containing surface layer has a thickness of about 10 nm, which agrees well with that of the pristine CAM (**Figure 1**). Moreover, the S, Ni+S, and Ni+S+P maps (**Figures 5e–g**,**l–n** and **S13–S15**) indicate that both S and P are enriched at the free surface (or interface with the thiophosphate SE). Notably, the S-containing layer is relatively thicker on the bare CAM (thinner layer formed on the surface of $LiNbO_3$-coated NCMs), which further emphasizes the positive effect that the coating has on interfacial side reactions.

High-angle annular dark-field (HAADF) STEM was employed to probe the structural stability of the near-surface regions of $LiNbO_3$@PC83, $LiNbO_3$@SC83, and SC83. **Figure 5o–r** shows the probed local area of the cycled $LiNbO_3$@PC83 at different magnifications. The images reveal that cracks formed around the grain boundaries (**Figure 5o**), even partially propagating to the surface, which agrees well with the particle fracture observed by cross-sectional SEM in **Figure 4f**. Distinct cracks were also observed in adjacent particles (**Figure S16**). In conventional LIBs, particle fracture can somewhat positively affect the CAM performance, because the liquid electrolyte is capable of accessing the newly formed cracks, thereby shortening the mean ion diffusion length.[44] However, in ASSBs, the ion diffusion/transport will be hindered as the SE is not mobile enough to infiltrate microcracks, and in the worst case, contact loss between CAM and SE occurs. Moreover, this unfavorable effect leads to a heterogeneous distribution of ionic diffusion over the particles, potentially accelerating crack propagation and aggravating bulk degradation. Several minor cracks were also observed on the nanometer level (**Figures 5p–r** and **S17**). Most of them formed along the (003) direction, parallel to the layering direction, while some also formed perpendicular to that direction. These cracks are most likely generated by tensile and shear stress derived from the lattice strain.[46] They clearly increase the lattice mismatch and cathode tortuosity, which in turn results in sluggish charge transport, thus sacrificing rate capability and stability at higher C-rates. As shown in **Figure 5s**, a surface rock-salt/cation mixing region of thickness around 2 nm is formed along the cracked grain boundary, although the CAM is not in direct contact with the SE.

Therefore, the transformation might be caused by local inhomogeneities in lithium distribution.[49] Overall, the STEM results match well with the previously stated hypotheses regarding the observed (in)stability. Moreover, the data in **Figure 5t**,**u** indicate that the formation of a rock-salt/cation mixing region at the outer surface of the $LiNbO_3$@PC83 and $LiNbO_3$@SC83 particles is either insignificant or not visible, while **Figure 5v** reveals the presence of a region consisting of rock-salt, cation mixed, and layered phases on the surface of SC83.

These observations underscore the occurrence of undesired interfacial reactions, which can be significantly suppressed with the presence of a conformal coating. Clearly, the protective effect of $LiNbO_3$ accounts for the superior cyclability of $LiNbO_3$@SC83, compared to uncoated SC83. This demonstrates that mitigation of mechanical degradation and surface instability are necessary in a concerted effort to improve upon the cycling performance of sulfide-based ASSBs.

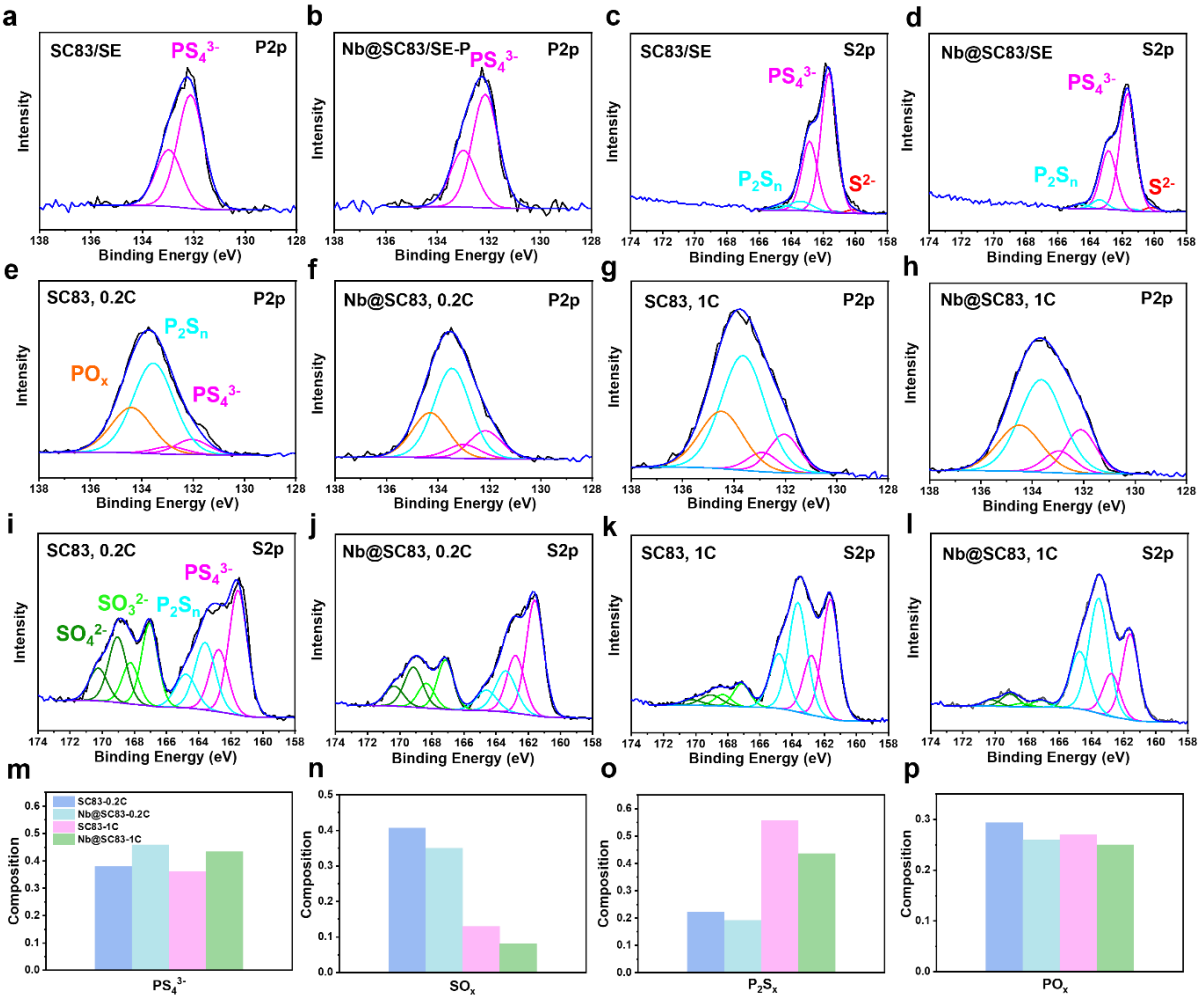

Figure 6. XPS data of the S 2p and P 2p regions collected from the SC83 and $LiNbO_3$@SC83 (referred to as Nb@SC83) cathodes in sulfide-based ASSBs (a–d) before and (e–l) after cycling at 0.2C (150 cycles) or 1C (1000 cycles). (m–p) Distribution of species from curve fitting.

The chemical changes at the CAM|SE interface due to side reactions were probed using XPS after 150 and 1000 cycles. **Figure 6a–d** shows detailed spectra of the S 2p and P 2p core-level regions of pristine (prior to cycling) SC83 and $LiNbO_3$@SC83 cathodes. The two prominent peaks at binding energies of 132.1 and 133 eV in the P 2p data correspond to the PS_4^{3-} species of the argyrodite SE.[10] The S 2p spectra show several doublets. Two intense peaks are visible at 161.7/162.9 eV, characteristics of PS_4^{3-}. The lower binding energy of 160.2 eV is indicative of the presence of minor Li_2S ("free" S^{2-}) impurities, while the peaks at 163.4/164.6 eV correspond to P_2S_x interfacial oxidation products.[6, 8, 5050] **Figure 6e–h** shows the P 2p spectra collected from the composite cathodes cycled at 0.2C (150 cycles) and 1C (1000 cycles). The main peaks at 132.1/133 eV, 133.5 eV, and 134.3 eV can be assigned to PS_4^{3-}, P_2S_x, and PO_x (or LiP_xO_y) species, respectively. Note that P_2S_x and PO_x originate from unwanted side reactions. The S 2p spectra in **Figure 6i–l** reveal four distinct doublets, belonging to PS_4^{3-} (161.6/162.7 eV), P_2S_x (163.4/164.6 eV), SO_3^{2-} (167.2/168.4 eV), and SO_4^{2-} (169.1/170.3eV), with the latter three species indicating electrochemical and/or chemical oxidation of SE upon long-term cycling.[51] It is worth noting that the coating is still tightly bound to the CAM particles after 150 cycles at 0.2C rate (**Figure S18**) and that Nb did not undergo notable changes in oxidation state, emphasizing its robustness and inert nature.

To clarify the severity of side reactions (between CAM and SE and SE and carbon black), the PS_4^{3-} and side product species were semi-quantitatively analyzed (**Figure 6m–p**). Evidently, the SE structure is better maintained when the SC83 particles are coated with a conformal $LiNbO_3$ layer. Besides, it can be seen that the oxygenated sulfur species are greatly decreased when the cells are operated at 1C (less time spent at high potentials). The presence of lower (relative) amounts of SO_x species appears to play an important role in stabilizing the cycling performance, as there are no major differences in oxygenated phosphorus species among the coated and uncoated cathodes.[52] The P_2S_x species apparently do not have a strong negative

effects on charge transport, while SO_x is detrimental to the interface stability.[6, 10] Collectively, the XPS data demonstrate that the coating is capable of mitigating, but not eliminating, adverse side reactions during battery operation. Minimal oxidative side products are detected with the $LiNbO_3$@SC83 cathodes upon cycling at high rates.

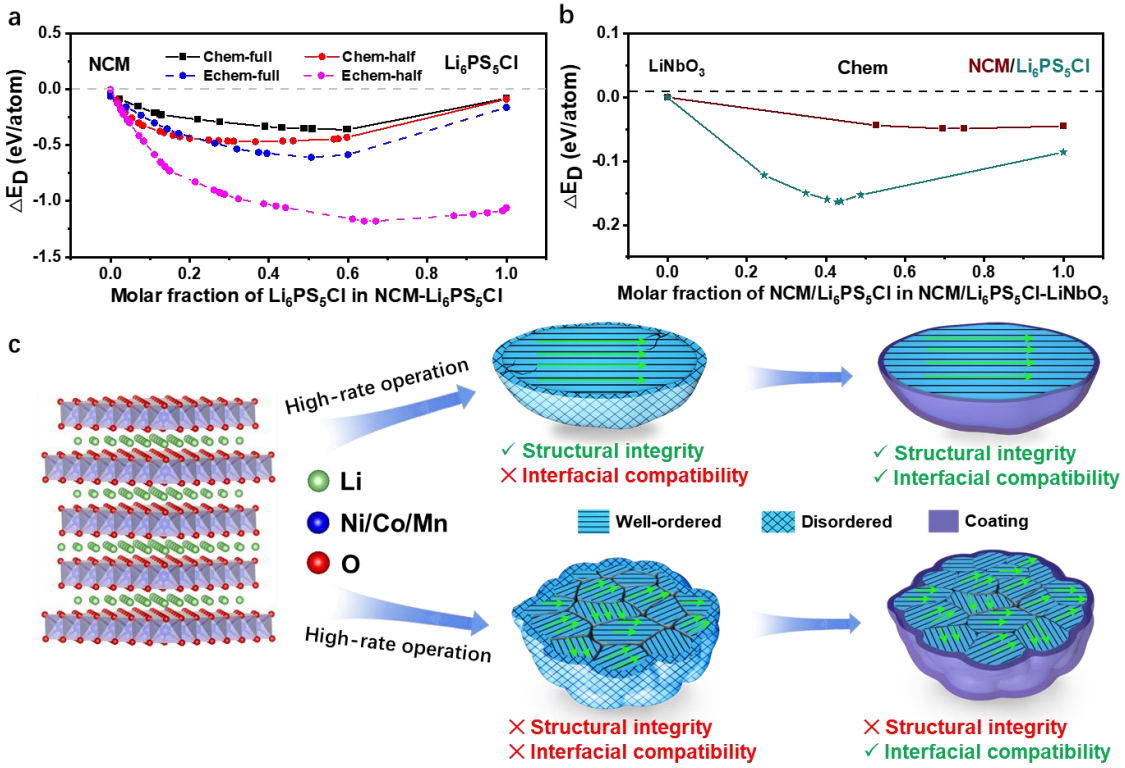

Figure 7. (a) Mutual chemical and electrochemical reaction energies at the fully and half lithiated states of NCM. (b) Mutual reaction energies between the CAM and the SE before and after $LiNbO_3$ coating. (c) Working principle and degradation pathways.

Finally, simulations were performed to verify the mitigation of interfacial failure by integrating the $LiNbO_3$ protective layer between CAM and SE. Specifically, the chemical and electrochemical reactions occurring between the NCM and the Li_6PS_5Cl were investigated by thermodynamic phase-equilibrium analysis, as shown in **Figure 7a**,**b**. The mutual reaction energy with the smallest magnitude was used to evaluate the reactivity at the CAM|SE interface. The chemical reaction energy reached −359 meV per atom at the fully lithiated state of NCM and decreased to −467 meV per atom for half-lithiated NCM. The electrochemical reaction energy reached −1178 meV per atom at the chemical potential of the half-lithiated NCM ($\mu_{\mathrm{Li}}^{\mathrm{open,H}} = -3.66$ eV), which is much lower than the chemical reaction energy. This indicates

that electrochemical reactions dominate the interfacial degradation and negatively affect the battery performance. The introduction of the $LiNbO_3$ coating strongly improves the compatibility by converting the highly reactive CAM|SE interface into two stable interfaces of $LiNbO_3$|CAM and $LiNbO_3$|SE with chemical reaction energies of −49 and −164 meV per atom, respectively. Notably, the passivating $LiNbO_3$|CAM and $LiNbO_3$|SE interfaces form due to the lower electronic transport through the protective coating. These results provide an explanation as to why less SE decomposition occurs and enhanced cyclability is achieved with ASSBs using the $LiNbO_3$@SC83.

Based on the aforementioned points, we summarize the major degradation pathways in **Figure 7c**. As can be seen, improved structural integrity and reduced tortuosity are key to achieving stable cyclability at fast charge/discharge. In the PC83 cells, both microcrack formation and surface reconstruction are unavoidable, significantly increasing the degree of tortuosity and blocking charge transport (across the interface, etc.), thus adversely affecting the electrochemical performance. Once an ionically conductive coating is applied to the PC83, the surface layer formation is largely suppressed. Therefore, the interfacial stability is improved, although the charge/discharge kinetics still suffers from intergranular particle cracking during cycling. By contrast, the structural integrity is drastically enhanced when SC83 is used in ASSBs, due to increased (bulk) robustness of single-crystalline CAM particles and reduced tortuosity for lithium transport. Accordingly, the cells exhibit better stability under high rate operation compared to PC83 and $LiNbO_3$@PC83. Utilizing $LiNbO_3$-coated SC83 eventually results in superior cyclability due to the reasons mentioned above.

Conclusions

In this work, we combined the favorable mechanical properties of single-crystalline Ni-rich NCM cathode materials with the protective nature of chemically inert and ionically conductive $LiNbO_3$ coatings to achieve a capacity retention of 88% after 1000 cycles at 1C rate. The designed material clearly outperforms both coated polycrystalline and uncoated single-crystalline counterparts, as well as similar systems reported in the literature. We also confirm the dual stabilization, which rests on a combination of mitigated mechanical degradation and

reduced interfacial reactivity. Notably, each stabilization mechanism on its own is insufficient to ensure stable long-term cycling performance. Polycrystalline NCM shows increased polarization due to particle fracture, which negatively affects charge transport and induces anisotropy, eventually accelerating intergranular cracking and mechanical degradation. Single-crystalline NCM with no protective coating is effective in alleviating mechanical stress while still suffering from interfacial side reactions. Introducing a protective coating aids in keeping the decomposition interphase formation to a minimum, thus allowing for stable cycling. Taken together, high structural stability, low tortuosity for lithium/electron transport, and good interfacial compatibility with the solid electrolyte are essential for achieving superior cycling performance in sulfide-based ASSBs, especially at high charge/discharge rates.

Experimental Section

Base Materials. SC83 powder ($d_{50} \approx 3$ μm) was provided by BASF SE. Li_6PS_5Cl and In metal were supplied by NEI Corp. and Sigma-Aldrich, respectively. The conductive carbon Super C65 (Imerys) was dried at 350 °C overnight before mixing with the Li_6PS_5Cl and CAM. 1 M lithium ethoxide solution was produced by reacting Li metal (Albemarle Germany GmbH) with absolute ethanol (Sigma-Aldrich; 99.8%). 0.5 M niobium ethoxide solution was prepared by dissolving $Nb(OCH_2CH_3)_5$ (99.95%) in absolute ethanol.

Preparation of PC83, $LiNbO_3$@SC83, and $LiNbO_3$@PC83. SC83 was regenerated first to remove surface impurities by heating at 750 °C for 3 h under O_2 flow. Then, 5.94 g of bare SC83 was dispersed into the lithium/niobium ethoxide solution with a molar ratio of 100:1. After solvent removal, the coated SC83 was calcined at 350 °C for 2 h under O_2 atmosphere to obtain the $LiNbO_3$@SC83.

The $Ni_{0.83}Co_{0.12}Mn_{0.05}(OH)_2$ precursor CAM (pCAM) was synthesized in a continuously stirred 5 L tank reactor by co-precipitation under N_2 atmosphere. Specifically, a 2 M (aqueous) solution of $NiSO_4 \cdot 6H_2O$, $CoSO_4 \cdot 7H_2O$, and $MnSO_4 \cdot H_2O$ (Ni:Co:Mn molar ratio of 83:12:5) was fed into the tank while maintaining the pH at 11.3 and the temperature at 50 °C. At the same time, an 8 M NaOH solution and a 5 M NH_3 solution were simultaneously injected into the reactor. The harvested pCAM was washed several times to remove residual species and then dried in

an oven at 120 °C for 12 h. Finally, a mixture of $Ni_{0.83}Co_{0.12}Mn_{0.05}(OH)_2$ and $LiOH \cdot H_2O$ (molar ratio of 1:1.03) was calcined at 500 °C for 10 h under O_2 atmosphere and then at 750 °C for 15 h. $LiNbO_3$@PC83 was prepared using the same procedure as for $LiNbO_3$@SC83.

Cell Assembly and Electrochemical Testing. A customized cell setup was used to study the electrochemical performance.[53] For assembly, 100 mg of Li_6PS_5Cl was compacted at 62 MPa to produce the separator pellet. Then, (12 ± 0.5) mg cathode composite and the In/InLi anode were added, followed by pressing the cell stack at 435 MPa. The cathode composite was prepared by milling CAM, Li_6PS_5Cl, and Super C65 (70:30:1 by weight) using 10 zirconia balls (Ø = 10 mm) in a high-energy ball mill (FRITSCH) at 140 rpm for 30 min in a sealed jar under Ar atmosphere. A pressure of 80 MPa was applied during electrochemical testing. Galvanostatic measurements were performed from 0.1C to 1C, with 1C = 190 mA/g, and at 45 °C in the potential window of 2.28–3.68 V vs. In/InLi (about 0.62 V vs. Li^+/Li) using a MACCOR battery test system.

Electrochemical impedance spectroscopy (EIS) was performed using a VMP3 multichannel potentiostat (BioLogic). The frequency ranged from 7 MHz to 10 mHz. A voltage amplitude of 7 mV was applied for collecting data.

Characterization. Scanning electron microscopy (SEM) measurements were performed on a Zeiss 1530 microscope equipped with a field emission source at an accelerating voltage of 10 kV. For cross-sectional SEM imaging, the composite cathodes were polished by Ar-ion milling using an IB-19510CP cross section polisher (JEOL). Note that the sample preparation requires inert conditions, such as in an Ar-filling glovebox, avoiding air exposure.

Ex situ transmission electron microscopy (TEM) was performed both on a Titan 80-300 image-corrected microscope (FEI) and on a Themis Z (Thermo Fisher Scientific) double-corrected microscope equipped with a Thermo-Fisher SuperX EDS detector. The acceleration voltage was set to 300 kV. Samples for TEM were prepared by the lift-out technique using a Ga FIB on STRATA and Helios G5 dual-beam systems (both from Thermo Fisher Scientific). They were milled at 30 kV, followed by final polishing at 2 kV to limit surface damage. Scanning TEM (STEM) images were collected using a HAADF detector.

For X-ray diffraction (XRD), samples were packed into 0.5 mm borosilicate capillaries

(Hilgenberg), and data were acquired in Debye-Scherrer geometry using a STOE Stadi-P diffractometer equipped with a Mo anode and a DECTRIS MYTHEN 1K detector. The instrumental parameter to peak broadening was determined by measuring a NIST Si 640f standard reference material. Rietveld refinement analysis of XRD data was performed using TOPAS Academic V7 software.

For *operando* XRD, the positive/negative caps and spacers of the coin cell casing were employed with a hole of 5 mm diameter in the middle, which was then sealed with Kapton foil to avoid air exposure. The cells were tested at a rate of C/20 using a Gamry Interface 1000 potentiostat. Patterns were collected in the range of $5° < 2\theta < 37°$ on a STOE Stadi-P diffractometer with a Mo anode and refined using the TOPAS-Academic v7 software.

X-ray photoelectron spectroscopy (XPS) measurements were performed on a SPECS system with a PHOIBOS 150 energy analyzer using monochromatic Al-Kα radiation. All samples were prepared in an Ar-filling glovebox (including transfer) to avoid oxidation. The C1s peak of adventitious carbon at 284.8 eV was utilized for calibration of binding energies. CasaXPS software was used for curve fitting, assuming Voigt profiles and Shirley-type background.

The Li, Ni, Co, Mn, and Nb contents were examined by inductively coupled plasma-optical emission spectroscopy (ICP-OES) using a Thermo Fisher Scientific iCAP 7600 DUO.

Simulation. The chemical stability between Li_6PS_5Cl and NCM/$LiNbO_3$ was estimated by the thermodynamic approximation method. The Li_6PS_5Cl-NCM/$LiNbO_3$ interface can be assumed as being a pseudo-binary system, with A: Li_6PS_5Cl and B: NCM/$LiNbO_3$, according to:

$$C_{\text{interface}}(c_A, c_B) = x\, c_A + (1-x) c_B, \quad (1)$$

where x is the molar fraction of Li_6PS_5Cl, and c_A and c_B represent the specific composition of Li_6PS_5Cl and NCM/$LiNbO_3$, respectively. The total energy of the pseudo-binary interface is described as a linear combination of Li_6PS_5Cl and NCM/$LiNbO_3$:

$$\Delta E_{\text{interface}}(c_A, c_B, x) = x\, E(c_A) + (1-x) E(c_B), \quad (2)$$

where $E(c_A)$ and $E(c_B)$ represent the ground state energy of Li_6PS_5Cl and NCM/$LiNbO_3$, respectively. The mutual reaction energy $\Delta E_{\text{D,mutual}}(c_A, c_B, x)$ can be calculated by constructing a pseudo-binary phase diagram and determining the ratio (x) that results in the most negative energy:

$$\Delta E_{\mathrm{D,mutual}}(c_{\mathrm{A}}, c_{\mathrm{B}}, x) = \min_{x\in[0,1]} \frac{1}{N}[E_{\mathrm{eq,interface}}(xc_{\mathrm{A}} + (1-x)c_{\mathrm{B}}) - xE_{\mathrm{D}}(c_A) - (1-x)E_{\mathrm{D}}(c_{\mathrm{B}})]. \quad (3)$$

Here, $E_{\mathrm{eq,interface}}$ is the reaction energy of the pseudo-binary phase, and $E_{\mathrm{D}}(c_{\mathrm{A}})$ and $E_{\mathrm{D}}(c_{\mathrm{B}})$ represent the decomposition energy of Li_6PS_5Cl and NCM/$LiNbO_3$, respectively. *N* is the number of atoms involved in the phase equilibrium used for normalization. The electrochemical stability of the Li_6PS_5Cl cathode interface was evaluated by inducing the (extra) applied Li chemical potential $\mu_{\mathrm{Li}}^{\mathrm{open},\emptyset}$:

$$\mu_{\mathrm{Li}}^{\mathrm{open},\emptyset} = \mu_{\mathrm{Li}}^{0} - e\emptyset, \quad (4)$$

where μ_{Li}^{0} and $\emptyset$ are the chemical potential of Li metal and the applied potential (referenced to Li metal), respectively. The mutual electrochemical reaction energy $\Delta E_{\mathrm{D,mutual}}^{\emptyset}(c_{\mathrm{A}}, c_{\mathrm{B}}, x, \emptyset)$ between the SE and CAM can be calculated by the following equation:

$$\Delta E_{\mathrm{D,mutual}}^{\emptyset}(c_{\mathrm{A}}, c_{\mathrm{B}}, x, \emptyset) = \min_{x\in[0,1]} \frac{1}{N_{\mathrm{gc}}}[E_{\mathrm{eq}}^{\emptyset}(xc_{\mathrm{A}} + (1-x)c_{\mathrm{B}}) - xE_{\mathrm{D}}^{\emptyset}(c_{\mathrm{A}}) - (1-x)E_{\mathrm{D}}^{\emptyset}(c_{\mathrm{B}})]. \quad (5)$$

It should be noted that the normalization factor N_{gc} in equation 5, unlike *N* in equation 3, is the total number of atoms excluding Li. The chemical potential μ_{Li} is applied at the fully ($\mu_{\mathrm{Li}}^{\mathrm{open,F}}$) and half ($\mu_{\mathrm{Li}}^{\mathrm{open,H}}$) lithiated states of NCM.

ASSOCIATED CONTENT

Supporting Information.

The Supporting Information is available free of charge at https://pubs.acs.org/acsnano.

SEM images and XRD patterns of the pristine and coated cathode particles; particle-size distributions; differential capacity curves and voltage profiles; additional cycling data; DRT patterns; elemental distribution maps; TEM images and XPS spectra of cycled cathodes; refined structural parameters; initial Coulomb efficiencies; comparison of electrochemical performances between our work and reported studies; and parameters derived from fitting the EIS data.

Notes

The authors declare no conflict of interest.

ACKNOWLEDGMENTS

This work was supported by BASF SE. The authors acknowledge the support from the Karlsruhe Nano Micro Facility (KNMFi, www.knmf.kit.edu), a Helmholtz research infrastructure at Karlsruhe Institute of Technology (KIT, www.kit.edu). The authors also thank the electron microscopy team at BASF SE as well as Thomas Bergfeldt and colleagues for conducting the ICP-OES analysis. Y.Y. acknowledges financial support from the National Natural Science Foundation of China (grant nos. 22261160570 and 21935009).

REFERENCES

1. Cui, Z.; Manthiram, A., Thermal Stability and Outgassing Behaviors of High-nickel Cathodes in Lithium-ion Batteries. *Angew. Chem. Int. Ed.* **2023**, *62*, e202307243.

2. Chen, Y.; Zhu, Y.; Zuo, W.; Kuai, X.; Yao, J.; Zhang, B.; Sun, Z.; Yin, J.; Wu, X.; Zhang, H.; Yan, Y.; Huang, H.; Zheng, L.; Xu, J.; Yin, W.; Qiu, Y.; Zhang, Q.; Hwang, I.; Sun, C.-J.; Amine, K.; Xu, G.-L.; Qiao, Y.; Sun, S.-G., Implanting Transition Metal into Li_2O-Based Cathode Prelithiation Agent for High-Energy-Density and Long-Life Li-Ion Batteries. *Angew. Chem. Int. Ed.* **2023**, *63*, e202316112.

3. Hu, J.; Li, W.; Duan, Y.; Cui, S.; Song, X.; Liu, Y.; Zheng, J.; Lin, Y.; Pan, F., Single-Particle Performances and Properties of $LiFePO_4$ Nanocrystals for Li-Ion Batteries. *Adv. Energy Mater.* **2016**, *7*, 1601894.

4. Feng, X.; Ren, D.; He, X.; Ouyang, M., Mitigating Thermal Runaway of Lithium-Ion Batteries. *Joule* **2020**, *4*, 743-770.

5. Zhao, W.; Wang, K.; Dubey, R.; Ren, F.; Brack, E.; Becker, M.; Grissa, R.; Seidl, L.; Pagani, F.; Egorov, K.; Kravchyk, K. V.; Kovalenko, M. V.; Yan, P.; Yang, Y.; Battaglia, C., Extending the high-voltage operation of Graphite/NCM811 cells by constructing a robust electrode/electrolyte interphase layer. *Mater. Today Energy* **2023**, *34*, 101301.

6. Wang, L.; Mukherjee, A.; Kuo, C.-Y.; Chakrabarty, S.; Yemini, R.; Dameron, A. A.;

DuMont, J. W.; Akella, S. H.; Saha, A.; Taragin, S.; Aviv, H.; Naveh, D.; Sharon, D.; Chan, T.-S.; Lin, H.-J.; Lee, J.-F.; Chen, C.-T.; Liu, B.; Gao, X.; Basu, S.; Hu, Z.; Aurbach, D.; Bruce, P. G.; Noked, M., High-energy all-solid-state lithium batteries enabled by Co-free $LiNiO_2$ cathodes with robust outside-in structures. *Nature Nanotech.* **2024**, *19*, 208-218.

7. Randau, S.; Weber, D. A.; Kötz, O.; Koerver, R.; Braun, P.; Weber, A.; Ivers-Tiffée, E.; Adermann, T.; Kulisch, J.; Zeier, W. G.; Richter, F. H.; Janek, J., Benchmarking the performance of all-solid-state lithium batteries. *Nature Energy* **2020**, *5*, 259-270.

8. Ma, Y.; Teo, J. H.; Kitsche, D.; Diemant, T.; Strauss, F.; Ma, Y.; Goonetilleke, D.; Janek, J.; Bianchini, M.; Brezesinski, T., Cycling Performance and Limitations of $LiNiO_2$ in Solid-State Batteries. *ACS Energy Lett.* **2021**, *6*, 3020-3028.

9. Tan, D. H. S.; Banerjee, A.; Chen, Z.; Meng, Y. S., From nanoscale interface characterization to sustainable energy storage using all-solid-state batteries. *Nature Nanotech.* **2020**, *15*, 170-180.

10. Ma, Y.; Teo, J. H.; Walther, F.; Ma, Y.; Zhang, R.; Mazilkin, A.; Tang, Y.; Goonetilleke, D.; Janek, J.; Bianchini, M.; Brezesinski, T., Advanced Nanoparticle Coatings for Stabilizing Layered Ni-Rich Oxide Cathodes in Solid-State Batteries. *Adv. Funct. Mater.* **2022**, *32*, 2111829.

11. Wang, C.; Yu, R.; Hwang, S.; Liang, J.; Li, X.; Zhao, C.; Sun, Y.; Wang, J.; Holmes, N.; Li, R.; Huang, H.; Zhao, S.; Zhang, L.; Lu, S.; Su, D.; Sun, X., Single crystal cathodes enabling high-performance all-solid-state lithium-ion batteries. *Energy Storage Mater.* **2020**, *30*, 98-103.

12. Han, Y.; Jung, S. H.; Kwak, H.; Jun, S.; Kwak, H. H.; Lee, J. H.; Hong, S. T.; Jung, Y. S., Single- or Poly-Crystalline Ni-Rich Layered Cathode, Sulfide or Halide Solid Electrolyte: Which Will be the Winners for All-Solid-State Batteries? *Adv. Energy Mater.* **2021**, *11*, 2100126.

13. Tian, R.; Wang, Z.; Liao, J.; Zhang, H.; Song, D.; Zhu, L.; Zhang, L., High-Voltage Stability of Small-Size Single Crystal Ni-Rich Layered Cathode for Sulfide-Based All-Solid-State Lithium Battery at 4.5 V. *Adv. Energy Mater.* **2023**, *13*, 2300850.

14. Han, F.; Zhu, Y.; He, X.; Mo, Y.; Wang, C., Electrochemical Stability of $Li_{10}GeP_2S_{12}$ and $Li_7La_3Zr_2O_{12}$ Solid Electrolytes. *Adv. Energy Mater.* **2016**, *6*, 1501590.

15. Zuo, T.-T.; Ruess, R.; Pan, R.; Walther, F.; Rohnke, M.; Hori, S.; Kanno, R.; Schröder, D.; Janek, J., A mechanistic investigation of the $Li_{10}GeP_2S_{12}|LiNi_{1-x-y}Co_xMn_yO_2$ interface stability

in all-solid-state lithium batteries. *Nature Commun.* **2021**, *12* (1), 6669.

16. Zhao, W.; Zou, L.; Zhang, L.; Fan, X.; Zhang, H.; Pagani, F.; Brack, E.; Seidl, L.; Ou, X.; Egorov, K.; Guo, X.; Hu, G.; Trabesinger, S.; Wang, C.; Battaglia, C., Assessing Long-Term Cycling Stability of Single-Crystal Versus Polycrystalline Nickel-Rich NCM in Pouch Cells with 6 mAh cm^{-2} Electrodes. *Small* **2022**, *18*, e2107357.

17. Liu, X.; Zheng, B.; Zhao, J.; Zhao, W.; Liang, Z.; Su, Y.; Xie, C.; Zhou, K.; Xiang, Y.; Zhu, J.; Wang, H.; Zhong, G.; Gong, Z.; Huang, J.; Yang, Y., Electrochemo-Mechanical Effects on Structural Integrity of Ni-Rich Cathodes with Different Microstructures in All Solid-State Batteries. *Adv. Energy Mater.* **2021**, *11*, 2003583.

18. Payandeh, S.; Goonetilleke, D.; Bianchini, M.; Janek, J.; Brezesinski, T., Single versus poly-crystalline layered oxide cathode materials for solid-state battery applications - a short review article. *Current Opin. Electrochem.* **2022**, *31*, 100877.

19. Kobayashi, S.; Watanabe, H.; Kato, T.; Mizuno, F.; Kuwabara, A., Atomic-Scale Observations of Oxygen Release Degradation in Sulfide-Based All-Solid-State Batteries with Layered Oxide Cathodes. *ACS Appl. Mater. Interfaces* **2022**, *14*, 39459-39466.

20. Ma, Y.; Zhang, R.; Ma, Y.; Diemant, T.; Tang, Y.; Payandeh, S.; Goonetilleke, D.; Kitsche, D.; Liu, X.; Lin, J.; Kondrakov, A.; Brezesinski, T., Interface and Electrode Microstructure Engineering for Optimizing Performance of the $LiNiO_2$ Cathode in All-Solid-State Batteries. *Chem. Mater.* **2024**, *36*, 2588-2598.

21. Ren, F.; Liang, Z.; Zhao, W.; Zuo, W.; Lin, M.; Wu, Y.; Yang, X.; Gong, Z.; Yang, Y., The nature and suppression strategies of interfacial reactions in all-solid-state batteries. *Energy Environ. Sci.* **2023**, *16*, 2579-2590.

22. Xiao, Y.; Miara, L. J.; Wang, Y.; Ceder, G., Computational Screening of Cathode Coatings for Solid-State Batteries. *Joule* **2019**, *3*, 1252-1275.

23. Kim, J. H.; Kim, H.; Choi, W.; Park, M.-S., Bifunctional Surface Coating of $LiNbO_3$ on High-Ni Layered Cathode Materials for Lithium-Ion Batteries. *ACS Appl. Mater. Interfaces* **2020**, *12*, 35098-35104.

24. Lee, J. S.; Park, Y. J., Comparison of $LiTaO_3$ and $LiNbO_3$ Surface Layers Prepared by Post- and Precursor-Based Coating Methods for Ni-Rich Cathodes of All-Solid-State Batteries. *ACS*

Appl. Mater. Interfaces **2021**, *13*, 38333-38345.

25. Bong, W. S. K.; Shiota, A.; Miwa, T.; Morino, Y.; Kanada, S.; Kawamoto, K., Effect of thickness and uniformity of $LiNbO_3$-coated layer on $LiNi_{0.5}Co_{0.2}Mn_{0.3}O_2$ cathode material on enhancement of cycle performance of full-cell sulfide-based all-solid-state batteries. *J. Power Sources* **2023**, *577*, 233259.

26. Peng, L.; Ren, H.; Zhang, J.; Chen, S.; Yu, C.; Miao, X.; Zhang, Z.; He, Z.; Yu, M.; Zhang, L.; Cheng, S.; Xie, J., $LiNbO_3$-coated $LiNi_{0.7}Co_{0.1}Mn_{0.2}O_2$ and chlorine-rich argyrodite enabling high-performance solid-state batteries under different temperatures. *Energy Storage Mater.* **2021**, *43*, 53-61.

27. Li, X.; Jin, L.; Song, D.; Zhang, H.; Shi, X.; Wang, Z.; Zhang, L.; Zhu, L., $LiNbO_3$-coated $LiNi_{0.8}Co_{0.1}Mn_{0.1}O_2$ cathode with high discharge capacity and rate performance for all-solid-state lithium battery. *J. Energy Chem.* **2020**, *40*, 39-45.

28. Murugan, S.; Zhang, R.; Janek, J.; Kondrakov, A.; Brezesinski, T., Facile solid-state synthesis of a layered Co-free, Ni-rich cathode material for all-solid-state batteries. *Chem. Commun.* **2023**, *59*, 10024-10027.

29. Morchhale, A.; Tang, Z.; Yu, C.; Farahati, R.; Kim, J.-H., Coating materials and processes for cathodes in sulfide-based all solid-state batteries. *Current Opin. Electrochem.* **2023**, *39*, 101251.

30. Kim, A.-Y.; Strauss, F.; Bartsch, T.; Teo, J. H.; Hatsukade, T.; Mazilkin, A.; Janek, J.; Hartmann, P.; Brezesinski, T., Stabilizing Effect of a Hybrid Surface Coating on a Ni-Rich NCM Cathode Material in All-Solid-State Batteries. *Chem. Mater.* **2019**, *31*, 9664-9672.

31. Islam, K.; Sultana, R.; Rakshit, A.; Goutam, U. K.; Chakraborty, S., X-ray reflectivity and X-ray photoelectron spectroscopy studies on reactively sputtered Nb_2O_5-based thin-film devices. *SN Appl. Sci.* **2020**, *2*, 782.

32. Tan, Z.; Chen, X.; Li, Y.; Xi, X.; Hao, S.; Li, X.; Shen, X.; He, Z.; Zhao, W.; Yang, Y., Enabling Superior Cycling Stability of $LiNi_{0.9}Co_{0.05}Mn_{0.05}O_2$ with Controllable Internal Strain. *Adv. Funct. Mater.* **2023**, *33*, 2215123.

33. Balamurugan, K.; Santhosh, S.; Mathankumar, M.; Subramanian, B., Electrochromic Performance of Sputtered NbTi-Based Mixed Metal Oxide Thin Films with a Metallic Seed

Layer. *ACS Omega* **2023**, *8*, 219-230.

34. Zhang, W.; Pan, X.; Long, P.; Liu, X.; Long, X.; Yu, Y.; Yi, Z., Platinum nanoparticles supported on defective tungsten bronze-type $KSr_2Nb_5O_{15}$ as a novel photocatalyst for efficient ethylene oxidation. *J. Mater. Chem. A* **2017**, *5*, 18998-19006.

35. Glass, A. M.; Nassau, K.; Negran, T. J., Ionic conductivity of quenched alkali niobate and tantalate glasses. *J. Appl. Phys.* **1978**, *49*, 4808-4811.

36. Yin, S.; Chen, H.; Chen, J.; Massoudi, A.; Deng, W.; Gao, X.; Zhang, S.; Wang, Y.; Lin, T.-W.; Banks, C. E.; Qiao, S.-z.; Zou, G.; Hou, H.; Ji, X., Chemical-Mechanical Effects in Ni-Rich Cathode Materials. *Chem. Mater.* **2022**, *34*, 1509-1523.

37. Li, J.; Yang, H.; Deng, Q.; Li, W.; Zhang, Q.; Zhang, Z.; Chu, Y.; Yang, C., Stabilizing Ni-rich Single-crystalline $LiNi_{0.83}Co_{0.07}Mn_{0.10}O_2$ Cathodes using Ce/Gd Co-doped High-entropy Composite Surfaces. *Angew. Chem. Int. Ed.* **2024**, *63*, e202318042.

38. Zhang, Q.; Chu, Y.; Wu, J.; Dong, P.; Deng, Q.; Chen, C.; Huang, K.; Yang, C.; Lu, J., Mitigating Planar Gliding in Single-Crystal Nickel-Rich Cathodes through Multifunctional Composite Surface Engineering. *Adv. Energy Mater.* **2024**, *14*, 2303764.

39. Liu, X.; Cheng, Y.; Su, Y.; Ren, F.; Zhao, J.; Liang, Z.; Zheng, B.; Shi, J.; Zhou, K.; Xiang, Y.; Zheng, J.; Wang, M.-S.; Huang, J.; Shao, M.; Yang, Y., Revealing the surface-to-bulk degradation mechanism of nickel-rich cathode in sulfide all-solid-state batteries. *Energy Storage Mater.* **2023**, *54*, 713-723.

40. Aktekin, B.; Sedykh, A. E.; Müller-Buschbaum, K.; Henss, A.; Janek, J., The Formation of Residual Lithium Compounds on Ni-Rich NCM Oxides: Their Impact on the Electrochemical Performance of Sulfide-Based ASSBs. *Adv. Funct. Mater.* **2024**, *34*, 2313252.

41. Ruess, R.; Schweidler, S.; Hemmelmann, H.; Conforto, G.; Bielefeld, A.; Weber, D. A.; Sann, J.; Elm, M. T.; Janek, J., Influence of NCM Particle Cracking on Kinetics of Lithium-Ion Batteries with Liquid or Solid Electrolyte. *J. Electrochem. Soc.* **2020**, *167*, 100532.

42. Zhang, Q.; Wang, Y.; Deng, Q.; Chu, Y.; Dong, P.; Chen, C.; Wang, Z.; Xia, Z. Yang, C., In situ and Real-time Monitoring the Chemical and Thermal Evolution of Lithium-ion Batteries with Single-crystalline Ni-rich Layered Oxide Cathode. *Angew. Chem. Int. Ed.* **2024**, *63*, e202401716.

43. Ryu, H.-H.; Park, K.-J.; Yoon, C. S.; Sun, Y.-K., Capacity Fading of Ni-Rich $Li[Ni_xCo_yMn_{1-x-y}]O_2$ ($0.6 \leq x \leq 0.95$) Cathodes for High-Energy-Density Lithium-Ion Batteries: Bulk or Surface Degradation? *Chem. Mater.* **2018**, *30*, 1155-1163.

44. Xu, Z.; Jiang, Z.; Kuai, C.; Xu, R.; Qin, C.; Zhang, Y.; Rahman, M. M.; Wei, C.; Nordlund, D.; Sun, C.-J.; Xiao, X.; Du, X.-W.; Zhao, K.; Yan, P.; Liu, Y.; Lin, F., Charge distribution guided by grain crystallographic orientations in polycrystalline battery materials. *Nat. Commun.* **2020**, *11*, 83.

45. Xia, S.; Mu, L.; Xu, Z.; Wang, J.; Wei, C.; Liu, L.; Pianetta, P.; Zhao, K.; Yu, X.; Lin, F.; Liu, Y., Chemomechanical interplay of layered cathode materials undergoing fast charging in lithium batteries. *Nano Energy* **2018**, *53*, 753-762.

46. Xu, G.-L.; Liu, X.; Zhou, X.; Zhao, C.; Hwang, I.; Daali, A.; Yang, Z.; Ren, Y.; Sun, C.-J.; Chen, Z.; Liu, Y.; Amine, K., Native lattice strain induced structural earthquake in sodium layered oxide cathodes. *Nat. Commun.* **2022**, *13*, 436.

47. Yu, H.; Wang, S.; Hu, Y.; He, G.; Bao, L. Q.; Parkin, I. P.; Jiang, H., Lithium-conductive $LiNbO_3$ coated high-voltage $LiNi_{0.5}Co_{0.2}Mn_{0.3}O_2$ cathode with enhanced rate and cyclability. *Green Energy Environ.* **2022**, *7*, 266-274.

48. Deng, Q.; Zhang, Q.; Chu, Y.; Xu, Y.; You, S.; Huang, K.; Yang, C.; Lu, J., Understanding improved stability of Co-free Ni-rich single crystal cathode materials by combined bulk and surface modifications. *Mater. Today* **2024**, *74*, 22-33.

49. Yan, P.; Zheng, J.; Gu, M.; Xiao, J.; Zhang, J.-G.; Wang, C.-M., Intragranular cracking as a critical barrier for high-voltage usage of layer-structured cathode for lithium-ion batteries. *Nat. Commun.* **2017**, *8*, 14101.

50. Walther, F.; Strauss, F.; Wu, X.; Mogwitz, B.; Hertle, J.; Sann, J.; Rohnke, M.; Brezesinski, T.; Janek, J., The Working Principle of a $Li_2CO_3/LiNbO_3$ Coating on NCM for Thiophosphate-Based All-Solid-State Batteries. *Chem. Mater.* **2021**, *33*, 2110-2125.

51. Wang, Y.; Lv, Y.; Su, Y.; Chen, L.; Li, H.; Wu, F., 5V-class sulfurized spinel cathode stable in sulfide all-solid-state batteries. *Nano Energy* **2021**, *90*, 106589.

52. Banerjee, A.; Wang, X.; Fang, C.; Wu, E. A.; Meng, Y. S., Interfaces and Interphases in All-Solid-State Batteries with Inorganic Solid Electrolytes. *Chem. Rev.* **2020**, *120*, 6878-6933.

53. Zhang, W.; Schröder, D.; Arlt, T.; Manke, I.; Koerver, R.; Pinedo, R.; Weber, D. A.; Sann, J.; Zeier, W. G.; Janek, J., (Electro)chemical expansion during cycling: monitoring the pressure changes in operating solid-state lithium batteries. *J. Mater. Chem. A* **2017**, *5*, 9929-9936.

TOC

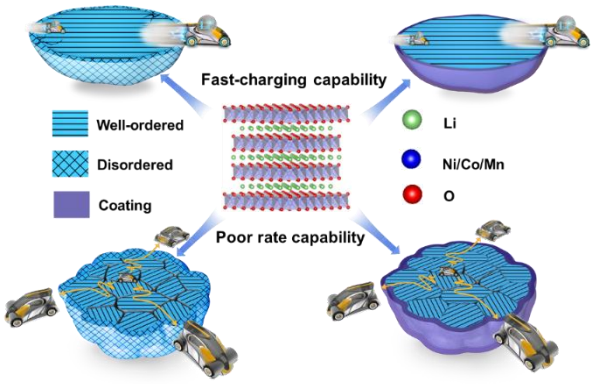
Fast-charging capability
Well-ordered
Disordered
Coating
Li
Ni/Co/Mn
O
Poor rate capability